Solar Energy 199 (2020): 864-871

DOI: https://doi.org/10.1016/j.solener.2020.02.082

Influence of Zn excess on compositional, structural and vibrational properties of $Cu_2ZnSn_{0.5}Ge_{0.5}Se_4$ thin films and their effect on solar cell efficiency

A. Ruiz-Perona[a], Y. Sánchez[b], M. Guc[b], L. Calvo-Barrio[c,d], T. Jawhari[c], J.M. Merino[a], M. León[a], R. Caballero[a,*]

[a]Universidad Autónoma de Madrid, Departamento de Física Aplicada, C/ Tomás y Valiente 7, 28049 Madrid, Spain

[b]IREC, Catalonia Institute for Energy Research, C/ Jardins de les Dones de Negre 1, Sant Adriá del Besòs, 08930 Barcelona, Spain

[c]Centres Científics i Tecnològics (CCiTUB), Universitat de Barcelona, C/ Lluis Solé i Sabaris, 08028 Barcelona, Spain

[d]Departament d'Enginyeria Electrònica i Biomèdica, IN2UB, Universitat de Barcelona, C/ Martí i Franqués 1, 08028 Barcelona, Spain

Abstract

The effect of Zn content on compositional, structural and vibrational properties of $Cu_2ZnSn_{1-x}Ge_xSe_4$ (CZTGSe, x ~ 0.5) thin films is studied. Kesterite layer is deposited by co-evaporation onto 5 x 5 cm^2 Mo/SLG substrate followed by a thermal treatment at maximum temperature of 480º C, obtaining areas with different composition and morphology which are due to the sample position in the co-evaporation system and to the non-uniform temperature distribution across the substrate. Kesterite layers with higher Zn amounts are characterized by lower Cu and Ge contents; however, a uniform Ge distribution through the absorber layer is detected in all cases. The excess Zn concentration leads to the formation of ZnSe secondary phase on the surface and in the bulk of the absorber as determined by Raman spectroscopy. When higher Ge content

and no ZnSe are present in the absorber layer, a compact structure is formed with larger grain size of kesterite. This effect could explain the higher V_{oc} of the solar cell. The Zn content does not affect the bandgap energy significantly (E_g near 1.3 eV), although the observed effect of Zn excess in CZTGSe results in a decreased device performance from 6.4 to 4.2 %. This investigation reveals the importance of the control of the off-stoichiometric CZTGSe composition during the deposition process to enhance solar cells properties.

Keywords: kesterite; ZnSe; Ge; solar cells

*Corresponding author: R. Caballero (raquel.caballero@uam.es), Phone: +34 91497 8559

1. Introduction

Thin film photovoltaic technology has reached efficiencies above 20%, making their performance comparable to Si-based solar cells. Thin films absorbers demonstrated efficiencies up to 29.1% for GaAs, 21.0% for CdTe and 23.35% for $Cu(In,Ga)Se_2$ (CIGSe) (Green et al., 2019). All these absorbers use scarce or toxic materials for their fabrication, so, in order to avoid this, $Cu_2ZnSn(S,Se)_4$ (CZTSSe) materials appear as an earth-abundant, non-toxic alternative, by replacing In and Ga of CIGSe absorbers with Zn and Sn. CZTSSe absorbers present good optoelectronic properties, direct bandgap, an absorption coefficient $\alpha > 10^4$ cm^{-1}, and tunable bandgap ranging from 1 eV to 2.25 eV (Schnabel et al., 2017; Garcia-Llamas et al., 2016) by modifying the material composition with the partial or total substitution of Sn with Ge and Se with S atoms. However, despite the similarities with $Cu(In,Ga)Se_2$ absorbers, the highest conversion efficiency for a CZTSSe device is of 12.6% (Wang et al., 2014), far from that achieved

by CIGSe-based solar cells. This technology development is held back due to the narrow phase stability of the material and the presence of secondary phases and defects, between other factors. Off-stoichiometric materials (Cu-poor, Zn-rich) have demonstrated better performances, but this is directly related to the reduction of the secondary phases formation. CZTSSe that are Cu-poor and Zn-rich are necessary to reduce the number of defect clusters [Cu_{Zn} + Sn_{Zn}] and [$2Cu_{Zn}$ + Sn_{Zn}], which affect kesterite solar cells negatively (Polizzotti et al., 2013; Chen et al., 2010; Chen et al., 2012; Schorr et al., 2020). When Zn/IV atomic ratio is above 1, not only kesterite phase is formed, but the excess of Zn promotes the formation of secondary phases (Just et al., 2016; Siebentritt and Schorr, 2012). ZnS and ZnSe are insulator phases which are easily formed during the synthesis (Pal et al., 2019) due to its low formation enthalpy (Mills, 1974). Besides, they cannot be easily detected since the X-ray diffraction peaks overlap with the main peaks of CZTS and CZTSe phases (Berg et al., 2014), so other techniques like Raman spectroscopy, measured under specific close to ZnSe resonant conditions, are needed for identification of this secondary phase (Schorr et al., 2020; Fairbrother et al., 2014).

The effect of Zn secondary phases on device performance has been studied in literature, and devices with high efficiencies and a large amount of Zn(S,Se) phase have been reported. However, different studies show that Zn(S,Se) can be detrimental for the cell depending on the location of the secondary phase. Grains of ZnSe on the front surface of the absorber reduce the device efficiency (Hsu et al.; 2013). Devices with large grains of ZnS in the bulk of the absorber show a decrease in performance (Just et al., 2011) while the presence of this secondary phase at the back contact has a negligible effect on the electrical properties (Shin et al., 2013). The amount of Zn excess is also a key factor, where increasing the Zn content above the stoichiometric point improves the device

performance, but further increasing of this amount leads to a drop in the efficiency (Min et al., 2018). Most of these studies agree on that the optimum Zn/Sn atomic ratio is between 1.1 and 1.2 for CZTSSe-based solar cells.

On the other hand, the addition of Ge into CZTSe kesterite lattice, forming $Cu_2ZnSn_{1-x}Ge_xSe_4$ (CZTGSe), has not only led to an increased bandgap energy, E_g, but also to an improved V_{oc}-deficit ($E_g/q - V_{oc}$, q: electron charge), which is the main limitation factor in this technology. But this enhancement of V_{oc}-deficit takes place for low Ge content, $x < 0.5$. The increase of Ge concentration above 0.5, results in a higher E_g, but also in a lower solar cell efficiency, that is similar to what is observed when S content increases (Kim et al., 2016a). It was reported (Neuschitzer et al., 2016) that the presence of deep defects at high Ge amounts, Sn_{Cu} and Ge_{Cu} antisite donor defects, may be the cause for solar cell deterioration. Collord et al. (Collord and Hillhouse, 2016) observed a lower performance of CZTGSe-based devices for $x > 0.5$ due to a deep defect located about 0.8 eV above the valence band and unfavorable band alignment. Highest efficiencies of 12.3 % have been achieved for CZTGSe solar cells with $x = 0.22$ and $E_g = 1.11$ eV (Kim et al., 2016b). The development of wide bandgap kesterite solar cells is very attractive and beneficial to use as a top cell in a tandem device or for semitransparent solar cells (Antunez et al., 2017; Yan et al., 2018). However, much more effort is necessary to increase E_g without deteriorating the device performance. For this purpose, it is necessary to increase Ge content, maintaining the optimal off-stoichiometric kesterite composition. Up to our knowledge, the effect of Zn has not been investigated when Ge concentration ($x \sim 0.5$) has been added into $Cu_2ZnSnSe_4$ lattice.

In this work, the effect of Zn content variation on CZTGSe absorber layer with x around 0.5 and grown by co-evaporation followed by a thermal treatment is investigated. It is demonstrated that the presence of ZnSe secondary phase detected by Raman

spectroscopy affects not only the structure of the kesterite layer, but also the device properties significantly. Two factors, higher Ge concentration and the absence of ZnSe phase, make possible to increase E_g and solar cell efficiency.

2. Experimental details

2.1. Deposition of $Cu_2Zn(Sn,Ge)Se_4$ thin films

$Cu_2ZnSn_{1-x}Ge_xSe_4$ (CZTGSe) thin films were deposited onto 5 x 5 cm^2 Mo/soda-lime glass (SLG) by co-evaporation of Cu, Sn, Ge, ZnSe and Se at nominal substrate temperature of 150º C. The substrate was rotated during deposition to improve the film uniformity. The co-evaporation process consisted of four stages. First, Se was evaporated onto Mo/SLG for 2 minutes. Secondly, all the elements were co-evaporated simultaneously. After that, in order to achieve a Cu-poor composition, Sn, Ge, ZnSe and Se were co-evaporated. Finally, only Sn, Ge and Se were evaporated for 2 minutes to reduce a possible Zn-rich CZTGSe surface. A similar procedure was used to deposit $Cu_2ZnSnSe_4$, as reported previously in (de la Cueva et al., 2018). The used low substrate temperature minimizes the losses of Sn and Ge. As-grown CZTGSe thin films were annealed in Ar atmosphere at a pressure of 9.5 x 10^4 Pa under excess of selenium. A two-stage annealing process was performed, at 330º C for 45 minutes and at 480º C for 15 minutes. For that, as-co-evaporated CZTGSe thin films were placed in a partially closed graphite box and inserted into a quartz tube furnace. In order to have an overpressure of selenium, pure elemental selenium (99.999 %) together with $GeSe_2$ were also supplied into the graphite container. The heating rate was of 20º C/min and the cooling rate was 10º C/min. Maximum temperatures lower than 500º C makes this

process compatible with the use of light polyimide substrates (Upilex, 2019), increasing the range of applications.

Table 1 summarizes the composition of four representative CZTGSe thin films after thermal treatment and coming from different regions of the mega-sample of 5 x 5 cm^2, as shown in the schematic diagram. Samples A and D in the mega-sample represent the farthest and the closest positions to the center of the co-evaporation system respectively. As it can be observed in Table 1, the composition is not so uniform despite the rotation of the substrate during the co-evaporation process. A tendency in the composition is detected in the mega-sample, Zn content increases and Ge and Cu concentrations decrease as we move away from the center of the system. This could be related with the different temperatures measured in the different regions along the substrate, of 125º C for A, around 145º C for B-C and approximately of 165º C for region D.

Table 1. Composition of the different regions of 5 x 5 cm^2-size CZTGSe absorber layer, as measured by EDX. A schematic diagram of the 5 x 5 cm^2-substrate indicating the four regions A, B, C and D analyzed in this study is also added.

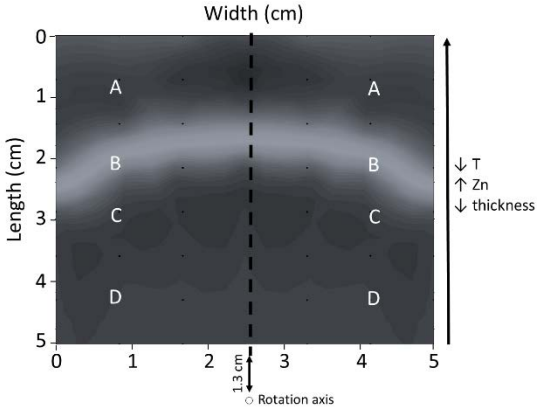

Sample	Cu (at %)	Zn (at %)	Sn (at %)	Ge (at %)	Se (at %)	Cu/(Zn+IV)	Zn/IV	Cu/IV	Ge/IV	Se/M
A	21.50	14.34	6.26	5.88	52.01	0.81	1.18	1.77	0.48	1.08
B	21.89	14.40	6.59	5.95	51.14	0.81	1.14	1.75	0.47	1.04
C	22.07	13.46	6.02	6.10	51.52	0.88	1.09	1.82	0.49	1.06
D	23.12	13.25	6.19	6.71	50.71	0.88	1.02	1.79	0.52	1.03

Note: IV = Sn + Ge; M = Cu + Zn + Sn + Ge

2.2. Device fabrication

Solar cells with the CZTGSe absorber layers were fabricated by using a CdS buffer layer of around 50 nm deposited by chemical bath deposition followed by 50 nm i-ZnO and 350 nm of In_2O_3:SnO_2 (ITO) layers deposited by DC-pulsed sputtering to act as a transparent conductive window layer. The absorber layer was etched with $KMnO_4/H_2SO_4$ before the buffer layer deposition. Prior to CdS deposition, a chemical treatment of the surface is performed and aims to eliminate ZnSe secondary phases. The chemical etching is carried out at room temperature using $KMnO_4$ (0.01M) as an oxidizing agent in a sulfuric acid medium (1M) during 40 seconds, after which the samples were rinsed and dried [López-Marino et al., 2013]. In order to remove elemental Se from the surface, the samples were placed in a 22% solution of $(NH_4)_2S$ for 2 min, rinsed and dried with an Ar gun and then placed in the chemical bath containing the CdS solution (Osinsky et al., 1997; Xie et al., 2014)".

The devices had neither grids nor antireflection coating layer. Moreover, no thermal treatment was carried out after finishing the solar cell devices.

2.3. Characterization techniques

The chemical composition was measured by energy dispersive X-ray spectroscopy (EDX) (Oxford instruments, model INCAx-sight) inside a Hitachi S-3000N scanning electron microscope (SEM). EDX measurements were carried out at 25 kV operating voltage, and the Cu K, Zn K, Sn L, Ge K and Se K lines were used for quantification. Grazing incidence X-ray diffraction (GIXRD) was performed to investigate the structural properties of the CZTGSe thin films. GIXRD data were collected with a PANAlytical X´Pert Pro MPD diffractometer, using CuK_α radiation and a multilayer mirror to produce a parallel beam. Detector scans with incident angles of 1º and 4º were carried out. Raman

scattering measurements of the CZTGSe surface were performed in back scattering configuration through the optical probe developed at IREC attached to the Horiba Jobin Yvon FHR640 monochromator coupled with a low noise CCD detector cooled at -70 °C. In this system, excitation and light collection were made through a macro optic system with a laser spot diameter of about 70 μm. The measurements were performed under 442 nm excitation wavelengths with laser power density ~ 80 W/cm^2. The spectra were corrected by imposing the Si first order Raman peak to 520 cm^{-1}. Raman measurements of kesterite thin films were carried out in different points on an area of 2.5 x 5 cm^2, the same as shown in Table 1. Solar cells were fabricated using the other half of the completed substrate, which can be considered similar to the one used for surface Raman characterization. In-depth Raman information were obtained by combining micro-Raman spectroscopy with AES experiment in order to investigate the presence of secondary phases through the absorber layer. Micro-Raman spectra were recorded with 2 excitation wavelengths, i.e. 458 and 532 nm, using a T64000 Jobin Yvon and a LabRam HR Horiba Jobin Yvon instruments, respectively. In the case of the former system, a laser power of the order of 50 μW was used at the sample with a x100 objective (analyzed area of about 0.5 μm), whereas the measurements obtained at 532 nm were realized using the DuoScan^{TM} mode of the LabRam system which permits to analyze areas of the order of 25μm x 25μm with a laser power of about 0.5 mW and x50 microscope objective.

Summarizing, several excitation wavelengths were used for the Raman study: blue laser lines, at 442 nm for the Raman mapping experiment and at 458 nm for the in-depth Raman analysis, were specially chosen in order to detect the ZnSe secondary phase since these excitation wavelengths are close to the resonance conditions for this phase and lead to strong Raman signal even at low concentrations of ZnSe. The 532 nm excitation wavelength was utilized to check the presence of other secondary phases, and to analyze

the spectra of the kesterite compound without the interference with the Raman signal of ZnSe.

In-depth chemical composition profiles were obtained by means of Auger electron spectroscopy (AES) using a Phi 670 Scanning Auger Nanoprobe. The excitation source was a field emission electron gun working at 10 keV and 10 nA, and scanning a surface of 15x15 microns to avoid inhomogeneities. Sputtering was done with Argon ions at 4 keV, and keeping vacuum under $9x10^{-9}$ Torr to prevent the reabsorption of the sputtered material. MultiPak v.8 and OriginLab 8.0 programs were utilized for data treatment and actual measurements of own standards were used as references for quantifications purposes. In parallel to the AES analysis, the in-depth Raman measurements were performed using 458 and 532 nm excitation wavelengths to investigate the presence of secondary phases through the absorber layer thickness. Scanning electron microscopy was used to study the morphology of the CZTGSe/Mo/glass structure using a Philips XL30S FEG scanning electron microscope at 5 kV operating voltage.

I-V characteristics were measured using a Sun 3000 class solar simulator (Abet Technologies Inc., Milford, Connecticut, USA). Measurements were carried out at 25º C and under air mass AM1.5 and 100 mW/cm^2 illumination. External quantum efficiency (EQE) measurements were performed using a Bentham PVE300 system (Bentham Instruments Ltd., Berkshire, UK) calibrated with a Si and Ge photodiode. Reversed voltage-biased EQE curves were collected by connecting a Keithley 2400 source meter (Keithley Instruments Inc., Cleveland, Ohio, USA) directly to the primary coil of the transformer and biasing the device at the desired voltage.

3. Results and discussion

Figure 1.a. shows GIXRD spectra (GI = 4º) of the complete devices using the absorber layer of the two extreme regions, A and D. The PDF data for tetragonal $Cu_2ZnSnSe_4$ (No. 04-010-6295) and tetragonal $Cu_2ZnGeSe_4$ (No. 04-012-7580) have been used for identification of the different phases. As it can be observed, kesterite phase is formed in both samples. Moreover, the reflections corresponding to Mo and ITO are detected because of the back contact and window layer of the solar cells. No other secondary phases can be detected, although the presence of ZnSe and $Cu_2(Sn,Ge)Se_3$ phases cannot be ruled out since their diffraction peaks coincide with those of CZTGSe. No significant differences are observed between both spectra. Figure 1.b. displays the 112 Bragg peak of both samples measured at GI = 1º and 4º. No clear shifts of the 112 diffraction peak are observed, suggesting a uniform distribution of Ge/(Ge+Sn) atomic ratio in the absorber layers.

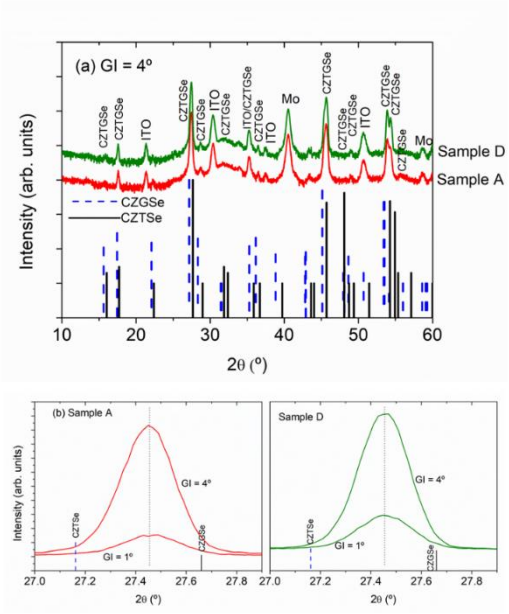

Figure 1. (a) Grazing incidence (GI = 4º) X-ray diffraction spectra of samples A and D implemented in the completed solar cell. (b) 112 Bragg peak for samples A and D using GI = 1º and 4º.

Raman scattering spectra of the bare absorber layers in the regions A, B, C and D of the half of the mega-sample were studied using the blue (442 nm) excitation wavelength, suitable for the fine ZnSe phase detection (Schorr et al., 2020; Fairbrother et al.; 2014). The Raman spectra presented in Figure 2.a. correspond to the main Raman bands of CZTGSe solid solutions (Garcia-Llamas et al., 2017), which confirms that kesterite is the main phase on the surface in all the regions. Here, both peaks with A-like symmetry and with E- or B-like symmetries were detected (Garcia-Llamas et al., 2017). As it was proposed in (Garcia-Llamas et al., 2017), the position of the most intense A^1-like symmetry peak can be used for the estimation of the Ge/(Ge+Sn) atomic ratio, which was found for all samples to lay close to 0.5, in good agreement with EDX analysis. Taking into account the solid solution influence, the bandwidth of the main Raman peak of CZTGSe was found to be relatively sharp (~ 10 cm^{-1}), indicating therefore a good crystalline quality of this phase. In addition to the main kesterite phase peaks, a clear intense band at 251 cm^{-1} is easily detected and is attributed to the ZnSe LO-symmetry peak (Dimitrievska et al., 2016). Presence of this secondary phase is further confirmed by the appearance of the second order (2LO) Raman mode at 502 cm^{-1} (Dimitrievska et al., 2016). The intensity of the ZnSe secondary phase was found to decrease as the Raman spectra were recorded from the edge to the center of the chamber (from A to D regions), and correlates quite well with the decrease in the Zn and Se contents as shown in Table 1. It is well known that using the 442 nm excitation wavelength will produce the Raman resonance effect of the ZnSe phase, which will therefore allow the detection of small amount of ZnSe. Thus, although in the case of sample A, where higher intensity of ZnSe peak was detected, the kesterite phase can be considered as the main phase, in accordance with GIXRD measurements. Finally, a mapping of the Raman signal was performed in order to check the distribution of the ZnSe secondary phase on the surface of mega-

sample (Figure 2.b). Here, a clear tendency of change of the ZnSe concentration in different areas of the mega-sample was detected. Moreover, a radial like distribution of the secondary phase was found in the sample, so for the further investigations it has been assumed that the other half of the mega-sample has a mirror-like distribution of this phase, as it was checked in previous experiments by EDX measurements.

.

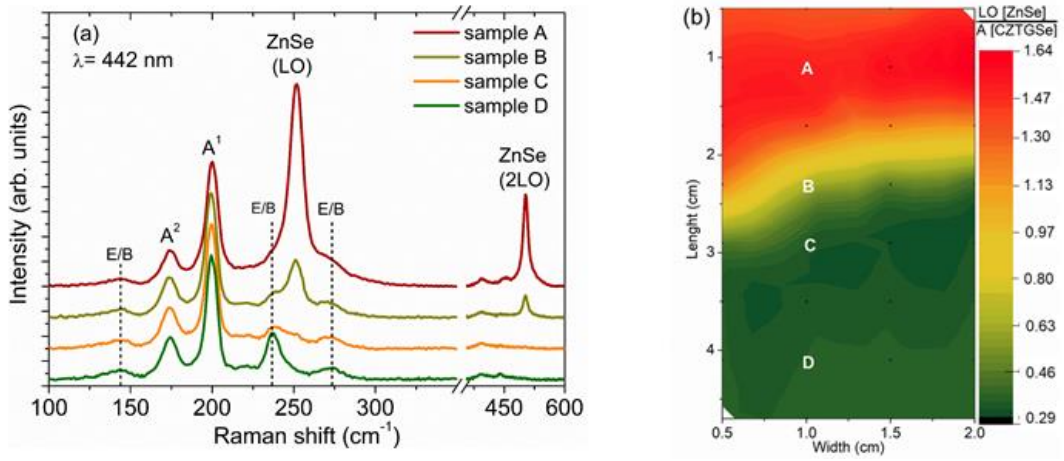

Figure 2. (a) Raman spectroscopy spectra of bare absorbers A, B, C and D using 442 nm wavelength. (b) Mapping of normalized main vibration modes of ZnSe to CZTGSe, LO[ZnSe]/A[CZTGSe], in a mega-sample size of 2.5 x 5 cm^2.

In-depth Raman measurements were combined with the AES in order to complete the study of the secondary phase distribution in the bulk of the absorber. Figure 3 shows Raman spectra measured under 458 nm excitation wavelength of completed devices of regions A and D measured at different depths after sputtering the devices surface for different amounts of time. All the spectra are characterized by the presence of the main peaks of the kesterite phase and by a dominant contribution at 301 and 603 cm^{-1}, related to the CdS buffer layer (Leite et al., 1969) for the first 10 minutes of sputtering (see Figure 3.a.). The spectrum measured on device A with 21 minutes sputter time shows an additional weak peak close to 250 cm^{-1}, that is identified with the main vibrational mode

of ZnSe. This measurement was repeated in different regions of sample A and the same result was obtained. However, this peak was not detected in sample D (see Figure 3.b.). Therefore, the presence of ZnSe was found not only on the surface of sample A, but also in the bulk of this absorber layer. Note, that for these measurements a micro-Raman system was used as it is described in the Experimental details section. Thus, the absence of the ZnSe peaks on the surface of the absorber A in the case of the in-depth Raman experiment, in contrast to the previously described surface analysis using the macro-Raman system, yields that this phase does not form a homogeneous layer, but rather small grains of ZnSe phase are expected through the whole volume of the absorber. Moreover, a surface etching before the buffer layer deposition could be the reason of the reduced ZnSe presence on the surface.

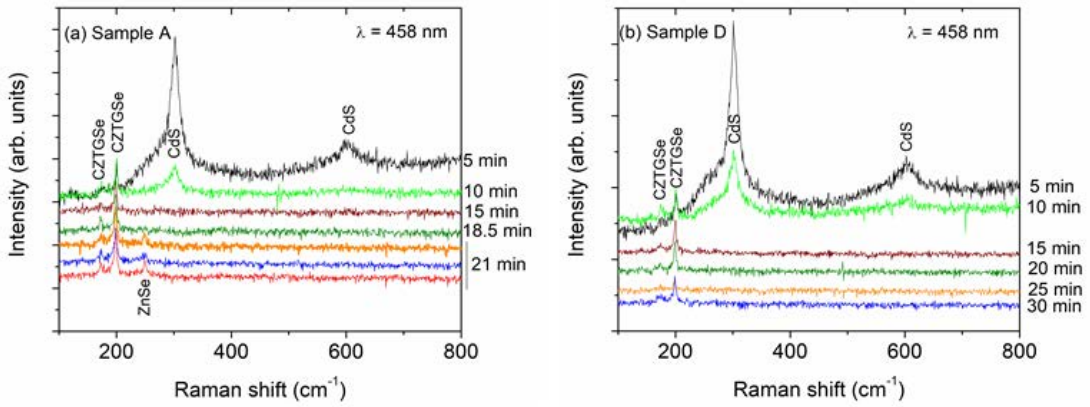

Figure 3. In-depth Raman spectroscopy spectra of (a) sample A and (b) sample D using 458 nm wavelength. At 21 minutes measurement was carried out in three different regions of sample A.

Additionally, to the secondary phase distribution the in-depth homogeneity of the main CZTGSe kesterite phase was determined by analyzing the Raman spectra measured under 532 nm excitation wavelength. Figure 4 displays Raman spectra of devices A and D, where the main peaks of kesterite are seen for both samples. In both sets of spectra a small

increase of the asymmetry at low wavenumbers of the main Raman peak can be observed, and can be partially related to the sputtering effect. However, the asymmetry is slightly more pronounced in case of device A. According to Dimitrievska et al. (Dimitrievska et al., 2014), this change of the shape of Raman peak could be also related to the phonon confinement effect. Thus, a slight decrease of the correlation length in-depth of the absorber layer A can be assumed from the Raman scattering analysis, while a slightly better homogeneity is observed in-depth of device D. At enough high Ar sputtering time (25 min for device A, and 30 min for device D) additional peaks at 173 and 245 cm^{-1} corresponding to the main vibrational modes of $MoSe_2$ (Caballero et al., 2014) were detected. Thus, a $MoSe_2$ phase is formed at the CZTGSe/Mo back interface.

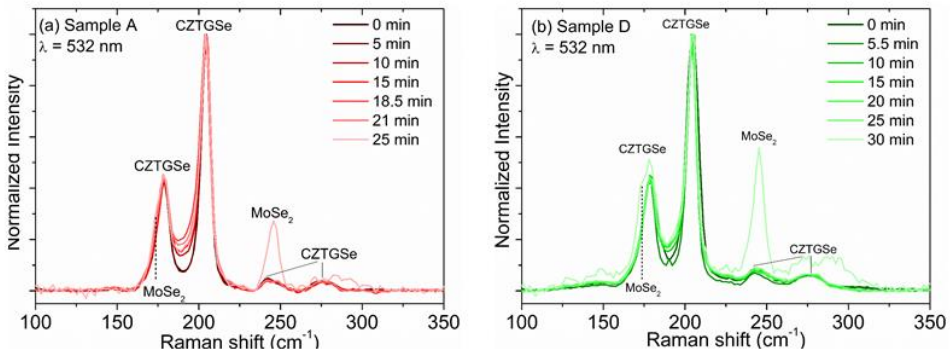

Figure 4. In-depth Raman spectroscopy spectra of (a) sample A and (b) sample D using 532 nm wavelength. The main modes corresponding to CZTGSe are detected together with those of $MoSe_2$.

Figure 5 shows AES depth profiles of the elements through representative Mo/CZTGSe/CdS/ZnO/ITO device structures of regions A and D, the same as investigated by in-depth Raman spectroscopy. In both cases a higher Se content is observed near the Mo back contact, which may be due to the formation of a $MoSe_2$ phase at the back interface as identified by in-depth Raman. A high oxygen content is also observed at the surface of the Mo layer, probably because of oxidation of the Mo back

contact. A higher Cu concentration at the surface is observed for device A. An opposite behavior is detected for Zn content with higher Zn signal next to the Mo contact, in agreement with the formation of a ZnSe phase in the bulk of the absorber A (see Figure 3.a.). However, a very uniform distribution of Cu and Zn through the kesterite layer D is observed, coinciding with the absence of secondary phases. A higher Ge/(Sn+Ge) atomic ratio is determined for the sample D compared to sample A, in accordance with EDX measurements.

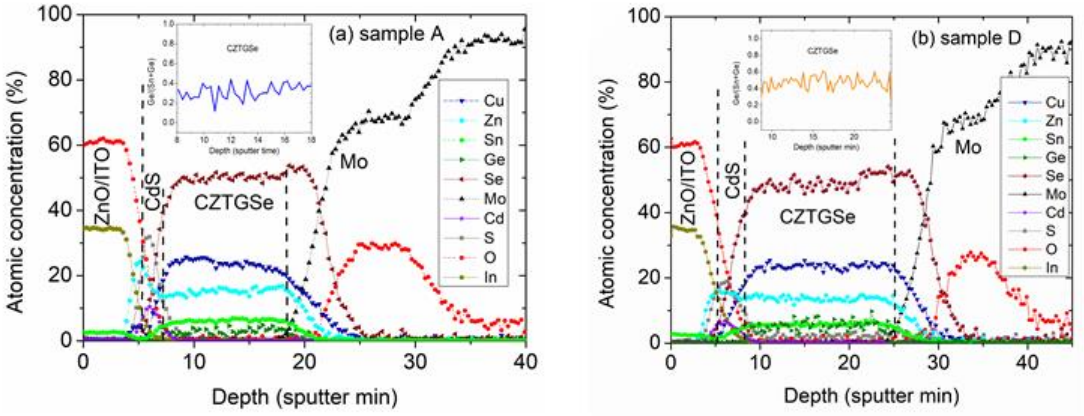

Figure 5. AES depth profiles of ITO/i-ZnO/CdS/CZTGSe/Mo solar cells using (a) sample A and (b) sample D as absorber layers. A zoom of Ge/(Sn + Ge) atomic ratio distribution through the kesterite layer is plotted.

Figure 6 shows cross-sectional SEM pictures of completed devices using absorbers of regions A and D. It is necessary to point out the very different structure of both kesterite thin films. The absorber layer of region A is characterized by very small grains, while that of region D has a much larger grain size with a more compact structure. Here it should be noted that the grains in the layer A became even smaller in the vicinity of the back contact, which can be a reason of the phonon confinement effect observed above in the in-depth Raman scattering analysis. Kim et al. (Kim et al., 2016a) showed that annealing environments containing $GeSe_2$ influenced the morphology of kesterite thin films by a

liquid-assisted grain growth that may act as a flux with a resulting formation of large CZTGSe grains. The presence of ZnSe secondary phase can promote the formation of smaller grains in the kesterite phase. First of all, the morphology can be conducted by the formation of two types of grains, the CZTGSe and ZnSe ones, which leads to small sizes of both of them. The second reason could be related to a significant change of the composition of the kesterite phase. As it is seen from Table 1, a higher Cu content is measured as well as higher Ge concentration is incorporated into the kesterite lattice for the D part of the mega-sample, which could lead to a bigger absorber grain size. Moreover, sample D is thicker than sample A, with 2.1 and 1.5 μm respectively, as shown in Figure 6. Therefore, not only the presence of ZnSe secondary phase depends strongly on the position of the sample during the co-evaporation process, but also the thickness and morphology of the kesterite layer. As mentioned above, the substrate was rotated during the deposition process, but it seems that the geometry of the chamber significantly affects the uniformity of the composition and thickness of the samples. The radial distribution of ZnSe phase in the mega-sample could also be related to the variation of substrate temperature with the distance to the center of the system, where the lamps are located. This seems to indicate that the increase in temperature lead to the elimination of ZnSe phase. However, the mega-sample of 5 x 5 cm^2 size was treated at 480º C after co-evaporation process. That means, once ZnSe is formed, this secondary phase is not reabsorbed in the kesterite by the thermal treatment, due to his high stability.

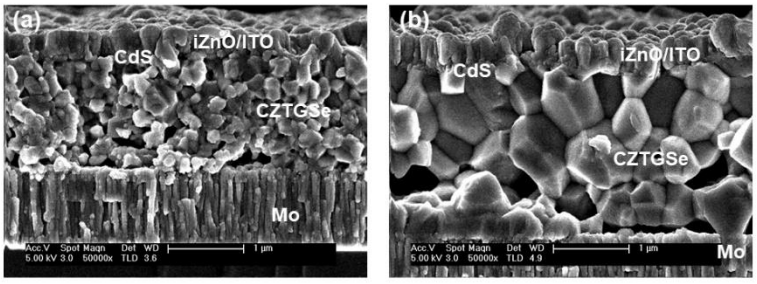

Figure 6. Cross-sectional SEM micrographs of the completed devices (a) A and (b) D.

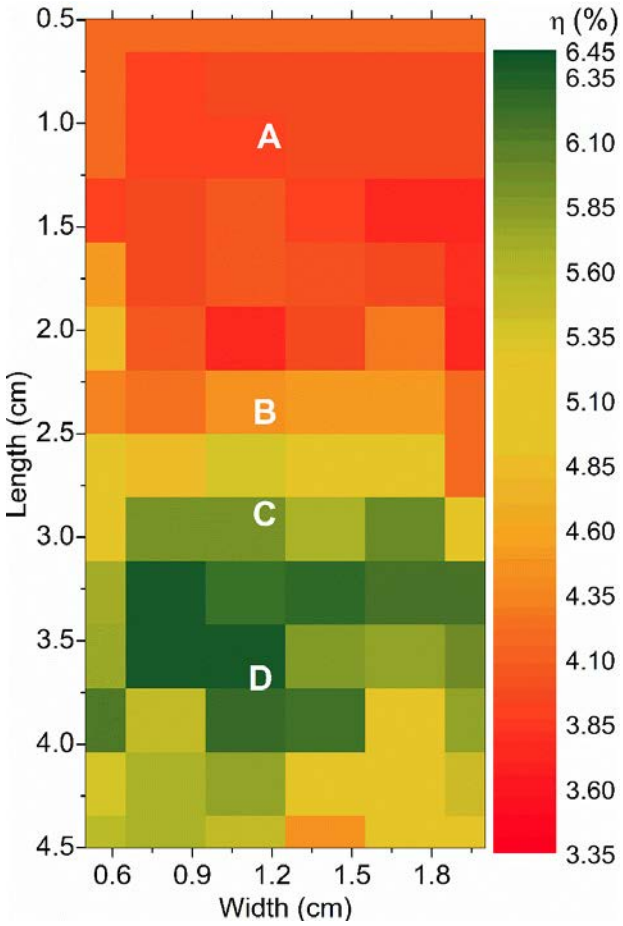

Figure 7. Mapping of efficiency of CZTGSe-based solar cells through the different regions A, B, C and D.

Table 2. Photovoltaic parameters and bandgap energy of CZTGSe solar cells.

Sample	V_{oc} (mV)	J_{sc} (mA/cm^2)	FF (%)	η (%)	E_g (eV)
A	443	17.3	54.5	4.2	1.27
D	510	22.4	56.3	6.4	1.28

Figure 7 shows an efficiency mapping through the different regions A, B, C and D. As expected, devices fabricated using absorbers A and D are the most different and they will be compared next. Table 2 shows the photovoltaic (PV) parameters of the best solar cells corresponding to samples A and D. All the PV parameters are better for the device D, achieving an efficiency of 6.4 %, while the best device A presents a 4.2 % performance.

Figure 8.a. displays EQE spectra for the devices shown in Table 2. Much higher EQE values in the whole wavelength have been obtained for device D, which agrees with its higher J_{sc}. Both solar cells present the same CdS buffer and i-ZnO/ITO layers. However, a lower EQE at around 500 nm is detected for sample A. The very different morphology of the absorbers could explain the different deposition of CdS on CZTGSe despite having used the same chemical bath process, which led to a higher CdS absorption when using sample A. In addition to that, a higher Cu content was measured at the surface of absorber A by AES, which could lead to a different heterointerface. Figure 8.b. shows the comparison between reverse-bias EQE measurements with the EQE without bias for the solar cells investigated. An increase in collection for the long wavelengths with negative bias (-1 V) is determined for both devices, being much more significant for the solar cell corresponding to sample A. The depletion width increases, and therefore, improves the electron collection generated deeper in the bulk of the CZTGSe by applying a reverse-bias voltage. This means that device A presents a poorer collection toward the back of the absorber layer (Scheer and Schock, 2011).

The optical band gap energy was extracted from the inflection point of the EQE spectra in the long wavelength. A E_g of 1.27 eV and 1.28 eV and V_{oc}-deficit of 0.84 V and 0.77 V have been determined for devices A and D respectively. The incorporation of Ge into kesterite lattice is again confirmed with the increased E_g. The slight increase of E_g for device D is in agreement with the higher Ge content, which leads to a higher V_{oc} and lower V_{oc}-deficit. The higher V_{oc} and decreased V_{oc}-deficit of device D may be also due to the uniform distribution of Zn through the absorber layer without the presence of ZnSe secondary phase that contributes to a better morphology with larger CZTGSe grains and dense structure. As mentioned above, the absorber layer is becoming thicker towards the center of the co-evaporation system. Although the absence of secondary phases and

enhanced morphology seem to be the most likely reasons of a performance improvement for device D, the effect of the thickness cannot be ruled out completely, especially on J_{sc}. Cu concentration can also play an important role on the device performance. However, a better efficiency and a slightly higher E_g are obtained for the device D with higher Cu concentration, which suggest that the ZnSe phase seems to be more decisive to enhance solar cell efficiency in the samples investigated. However, it is difficult to correlate some changes only to the composition of one of the elements, as this change will definitely influence the composition of the others elements.

In this work, a pretty uniform distribution of Ge through the absorber layer has been determined. A further investigation will consider the control of Ge depth-profile to enhance V_{oc} and J_{sc}, and therefore device performance, with the subsequent influence on composition and structure.

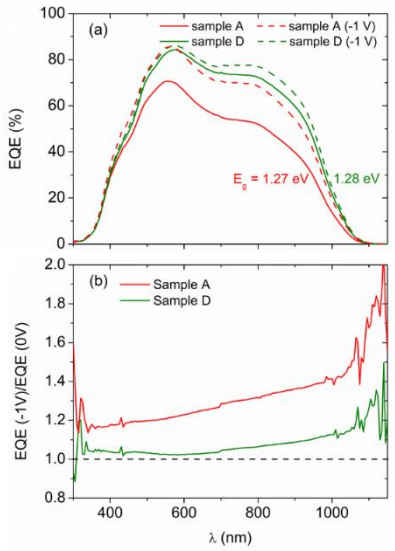

Figure 8. (a) Unbiased and reverse bias EQE curves and (b) ratios between voltage biased (-1 V) and unbiased EQE for the solar cells of Table 2.

5. Conclusions

CZTGSe thin films have been grown by co-evaporation at 150º C followed by a subsequent annealing at 480º C. A CZTGSe mega-sample of 5 x 5 cm^2 size with different Zn concentration has been investigated. A study of the Zn content on the properties of kesterite layers and final solar cell devices has been performed. An excess of Zn content is accompanied by a lower Ge and Cu concentrations. Samples with more than 14 at % Zn led to the formation of ZnSe secondary phase, which has been detected not only on the surface, but also in the bulk of the absorber layer by Raman scattering spectroscopy. An in-plane radial distribution of ZnSe secondary phase was detected through the mega-sample. Absorber layers without secondary phases showed larger grains and more compact structure. The excess Zn content reduced all the PV parameters and in particular, device performance from 6.4 to 4.2 % with similar bandgap energies near 1.3 eV. These results achieved at low temperature shows the potential of CZTGSe material to be deposited on light and flexible polyimide substrates.

Acknowledgements

This work was supported by Spanish Ministry of Science, Innovation and Universities Project WINCOST (ENE2016-80788-C5-2-R) and European Project INFINITE CELL (H2020-MSCA-RISE-2017-777968). ARP also acknowledges financial support from Community of Madrid within Youth Employment Program (PEJD-2017-PRE/IND-4062). MG acknowledges the financial support from ACCIÓ-Generalitat de Catalunya within the TECNIOspring Plus fellowship (TECSPR18-1-0048).

References

Antunez, P.D., Bishop, D.M., Luo, Y., Haight, R., 2017. Efficient kesterite solar cells with high open-circuit voltage for applications in powering distributed devices. Nature Energy 2, 884-890. DOI: 10.1038/s41560-017-0028-5.

Berg, D. M., Arasimowicz, M., Djemour, R., Gütay, L., Siebentritt, S., Schorr, S., Fontané, X., Izquierdo-Roca, V., Pérez-Rodriguez, A., Dale, P.J., 2014. Discrimination and detection limits of secondary phases in Cu_2 $ZnSnS_4$ using X-ray diffraction and Raman spectroscopy. Thin Solid Films 569, 113–123. DOI: 10.1016/j.tsf.2014.08.028.

Caballero, R., Nichterwitz, M., Steigert, A., Eicke, A., Lauermann, I., Schock, H.W., Kaufmann, C.A., 2014. Impact of Na on $MoSe_2$ formation at the CIGSe/Mo interface in thin-film solar cells on polyimide foil at low process temperatures. Acta Materialia 63, 54-62. DOI: 10.1016/j.actamat.2013.09.051.

Chen, S., Gong, X., Walsh, A., Wei, S.H., 2010. Defect physics of the kesterite thin-film solar cell absorber Cu_2ZnSnS_4, Appl. Phys. Lett. 96, 021902. DOI: 10.1063/1.3275796.

Chen, S., Wang, L.W., Walsh, A., Gong, X., Wei, S.H., 2012. Abundance of Cu_{Zn} + Sn_{Zn} and $2Cu_{Zn}$ + Sn_{Zn} defect clusters in kesterite solar cells, Appl. Phys. Lett. 101, 223901. DOI: 10.1063/1.4768215.

Collord, A.D., Hillhouse, H.W, 2016. Germanium Alloyed Kesterite Solar Cells with Low Voltage Deficits, Chemistry of Materials 28, 2067-2073. DOI: 10.1021/acs.chemmater.5b04806.

de la Cueva, L. , Sánchez, Y., Calvo-Barrio, L., Oliva, F., Izquierdo-Roca, V., Khelifi, S., Bertram, T., Merino, J.M., León, M., Caballero, R., 2018. Sulfurization of co-

evaporated $Cu_2ZnSnSe_4$ thin film solar cells: The role of Na, Sol. Energy Mater. Sol. Cells 186, 115-123. DOI : 10.1016/j.solmat.2018.06.015.

Dimitrievska, M., Fairbrother, A., Perez-Rodriguez, A., Saucedo, E., Izquierdo-Roca, V., 2014. Raman scattering crystalline assessment of polycrystalline Cu_2ZnSnS_4 thin films for sustainable photovoltaic technologies: Phonon confinement model, Acta Materialia 70, 272–280. DOI: 10.1016/j.actamat.2014.02.035.

Dimitrievska, M., Xie, H., Jackson, A. J., Fontané, X., Espindola-Rodriguez, M., Saucedo, E., Perez-Rodriguez, A., Walsh, A., Izquierdo-Roca, V, 2016. Resonant Raman scattering of ZnS_xSe_{1-x} solid solutions: the role of S and Se electronic states, Phys. Chem. Chem. Phys. 18, 7632-7640. DOI: 10.1039/C5CP04498G.

Fairbrother, A., Fontané, X., Izquierdo-Roca, V., Placidi, M., Sylla, D., Espindola-Rodriguez, M., López-Marino, S., Pulgarín, F. A., Vigil-Galán, O., Pérez-Rodríguez, A., Saucedo, E, 2014. Secondary phase formation in Zn-rich $Cu_2ZnSnSe_4$-based solar cells annealed in low pressure and temperature conditions. Prog. Photovolt: Res. Appl. 22, 479-487. DOI: 10.1002/pip.2473.

Garcia-Llamas, E., Merino, J.M., Serna, R., Fontané, X., Victorov, I.A., Pérez-Rodríguez, A., León, M., Bodnar, I.V., Izquierdo-Roca, V., Caballero, R, 2016. Wide band-gap tuning $Cu_2ZnSn_{1-x}Ge_xS_4$ single crystals: Optical and vibrational properties. Sol. Energy Mater. Sol. Cells 158, 147–153. DOI: 10.1016/j.solmat.2015.12.021.

Garcia-Llamas, E., Guc, M., Bodnar, I.V., Fontané, X., Caballero, R., Merino J.M., León, M., Izquierdo-Roca, V., 2017. Multiwavelength excitation Raman scattering of $Cu_2ZnSn_{1-x}Ge_x(S,Se)_4$ single crystals for earth abundant photovoltaic applications. Journal of Alloys and Compounds 692, 249-256. DOI: 10.1016/j.jallcom.2016.09.035.

Green, M.A., Dunlop, E.D., Levi, D.H., Hohl-Ebinger, J., Yoshita, M., Ho-Baillie, A. W.Y, 2019. Solar cell efficiency tables (version 54). Prog. Photovolt. Res. Appl., 27, 565–575. DOI: 10.1002/pip.3171.

Hsu, W.C., Repins, I., Beall, C., DeHart, C., Teeter, G., To, B., Yang, Y., Noufi, R, 2013. The effect of Zn excess on kesterite solar cells, Sol. Energy Mater. Sol. Cells 113, 160–164. DOI: 10.1016/j.solmat.2013.02.015.

Just, J., Lützenkirchen-Hecht, D., Frahm, R., Schorr, S., Unold, T, 2011. Determination of secondary phases in kesterite Cu_2ZnSnS_4 thin films by x-ray absorption near edge structure analysis, Appl. Phys. Lett. 99, 262105. DOI: 10.1063/1.3671994.

Just J., Sutter-Fella, C.M., Lützenkirchen-Hecht, D., Frahm, R., Schorr, S., Unold, T, 2016. Secondary phases and their influence on the composition of the kesterite phase in CZTS and CZTSe thin films, Phys. Chem. Chem. Phys. 18, 15988–15994. DOI: 10.1039/C6CP00178E.

Kim, S., Kim, K.M., Tampo, H., Shibata, H., Matsubara, K., Niki, S, 2016. Ge-incorporated $Cu_2ZnSnSe_4$ thin-film solar cells with efficiency greater than 10%, Sol. Energy Mater. Sol. Cells 144, 488-492. DOI: 10.1016/j.solmat.2015.09.039.

Kim, S., Kim, K.M., Tampo, H., Shibata, H., Niki, S, 2016b. Improvement of voltage deficit of Ge-incorporated kesterite solar cell with 12.3% conversion efficiency Appl. Phys. Express 9, 102301. DOI: 10.7567/APEX.9.102301.

Leite, R.C.C., Scott, J.F., Damen, T.C., 1969. Multiple-phonon resonant Raman scattering in CdS, Phys. Rev. Lett. 22 780-782. DOI: 10.1103/PhysRevLett.22.780.

López-Marino, S., Sánchez, Y., Placidi, M., Fairbrother, A., Espíndola-Rodríguez, M., Fontané, X., Izquierdo-Roca, V., López-García, J., Calvo-Barrio, L., Pérez-Rodríguez, A., Saucedo, E., 2013. ZnSe etching of Zn-rich $Cu_2ZnSnSe_4$: an oxidation

route for improved solar-cell efficiency, Chem. Eur. J. 19, 14814-14822. DOI : 10.1002/chem.201302589.

Mills, K. C., 1974. Thermodynamic data for inorganic sulphides, selenides and tellurides, Butterworths, London.

Min, X., Shi, J., Guo, L., Yu, Q., Zhang, P., Tian, Q., Li, D., Luo, Y., Wu, H., Meng, Q., Wu, S.,2018. Regulation of Zn/Sn ratio in kesterite absorbers to boost 10% efficiency of $Cu_2ZnSn(S,Se)_4$ solar cells, Chin. Phys. B 27, 016402. DOI: 10.1088/1674-1056/27/1/016402.

Neuschitzer, M., Marquez, J., Giraldo, S., Dimitrievska, M., Placidi, M., Forbes, I., Izquierdo-Roca, V., Pérez-Rodríguez, A., Saucedo, E., 2016. V_{oc} Boosting and Grain Growth Enhancing Ge-Doping Strategy for $Cu_2ZnSnSe_4$ Photovoltaic Absorbers. The Journal of J. Phys. Chem. C 120, 9661-9670. DOI: 10.1021/acs.jpcc.6b02315.

Osinsky, A., Qiu, Y., Mahan, J., Temkin, H., Gurevich, S.A., Nesterov, S.I., Tanklevskaia, E.M., Tretyakov, V., Lavrova, O.A., Skopina, V.I., 1997. Novel wet chemical etch for nanostructures based on II-VI compounds. Appl. Phys. Lett. 71, 509-511. DOI: 10.1063/1.119593.

Pal, K., Singh, P., Bhaduri, A., Thapa, K.B., 2019. Current challenges and future prospects for a highly efficient (>20%) kesterite CZTS solar cell: A review, Sol. Energy Mater. Sol. Cells 196, 138–156. DOI: 10.1016/j.solmat.2019.03.001.

Polizzotti, A., Repins, I.L., Noufi, R., Wei, S.H., Mitzi, D.B., 2013. The state and future prospects of kesterite photovoltaics, Energy Environ. Sci. 6, 3171–3182. DOI: 10.1039/C3EE41781F.

Schnabel, T., Seboui, M., Ahlswede, E., 2017. Band Gap Tuning of $Cu_2ZnGeS_xSe_{4-x}$ absorbers for thin-film solar cells. Energies 10, 1813 (1-9). DOI: 10.3390/en10111813.

Scheer, R., Schock, H.W., 2011. Chalcogenide Photovoltaics, Wiley-VCH Verlag, Weinheim, Germany.

Schorr, S., Gurieva, G., Guc, M., Dimitrievska, M., Pérez-Rodríguez, A., Izquierdo-Roca, V., Schnohr, C. S., Kim, J., Jo, W., Merino, J.M., 2020. Point defects, compositional fluctuations and secondary phases in non-stoichiometric kesterites, J. Phys. Energy 2, 012002/40. DOI: 10.1088/2515-7655/ab4a25.

Shin, B., Gunawan, O., Zhu, Y., Bojarczuk, N. A., Chey, S. J., Guha, S, 2013. Thin film solar cell with 8.4% power conversion efficiency using an earth-abundant Cu_2ZnSnS_4 absorber, Prog. Photovolt. Res. Appl. 21, 72–76. DOI: 10.1002/pip.1174.

Siebentritt, S., Schorr, S., 2012. Kesterirtes- a challenging material for solar cells, Prog. Photovolt. Res. Appl. 20, 512-519. DOI: 10.1002/pip.2156.

Wang, W., Winkler, M.T., Gunawan, O., Gokmen, T., Todorov, T. K., Zhu, Y., Mitzi, D. B., 2014. Device Characteristics of CZTSSe thin-film solar cells with 12.6% Efficiency, Adv. Energy Mater. 4, 1301465. DOI: 10.1002/aenm.201301465.

Xie, H., Sánchez, Y., López-Marino, S., Espíndola-Rodríguez, M., Neuschitzer, M., Sylla, D., Fairbrother, A., Izquierdo-Roca, V., Pérez-Rodríguez, A., Saucedo, E., 2014. Impact of Sn(S,Se) secondary phases in $Cu_2ZnSn(S,Se)_4$ solar cells: a chemical router for their selective removal and absorber surface passivation. ACS Appl. Mater. Interfaces 6, 12744-12751. DOI: 10.1021/am502609c.

Yan, C., Huang, J., Sun, K., Johnston, S., Zhang, Y., Sun, H., Pu, A., He, M., Liu, F., Eder, K., Yang, L., Cairney, J.M., Ekins-Daukes, N.J., Hameiri, Z., Stride, J.A., Chen, S., Green, M.A., Hao, X., 2018. Cu_2ZnSnS_4 solar cells with over 10% power conversión efficiency enabled by heterojunction heat treatment, Nature Energy 3, 764-772. DOI: 10.1038/s41560-018-0206-0.

Upilex, Ultra heat-resistance films, http://www.upilex.jp/en/upilex.html

Figure captions

Figure 1. (a) Grazing incidence (GI = 4º) X-ray diffraction spectra of samples A and D implemented in the completed solar cell. (b) 112 Bragg peak for samples A and D using GI = 1º and 4º.

Figure 2. (a) Raman spectroscopy spectra of bare absorbers A, B, C and D using 442 nm wavelength. (b) Mapping of normalized main vibration modes of ZnSe to CZTGSe, LO[ZnSe]/A[CZTGSe], in a mega-sample size of 2.5 x 5 cm^2.

Figure 3. In-depth Raman spectroscopy spectra of (a) sample A and (b) sample D using 458 nm wavelength. At 21 minutes measurement was carried out in three different regions of sample A.

Figure 4. In-depth Raman spectroscopy spectra of (a) sample A and (b) sample D using 532 nm wavelength. The main modes corresponding to CZTGSe are detected together with those of $MoSe_2$.

Figure 5. AES depth profiles of ITO/i-ZnO/CdS/CZTGSe/Mo solar cells using (a) sample A and (b) sample D as absorber layers. A zoom of Ge/(Sn + Ge) atomic ratio distribution through the kesterite layer is plotted.

Figure 6. Cross-sectional SEM micrographs of the completed devices (a) A and (b) D.

Figure 7. Mapping of efficiency of CZTGSe-based solar cells through the different regions A, B, C and D.

Figure 8. (a) Unbiased and reverse bias EQE curves and (b) ratios between voltage biased (-1 V) and unbiased EQE for the solar cells of Table 2.